

## Temperature Measurements of Liquid Flat Jets in Vacuum

Yi-Ping Chang,<sup>1</sup> Zhong Yin,<sup>2, a)</sup> Tadas Balciunas,<sup>1, 2</sup> Hans Jakob Wörner,<sup>2</sup> and Jean-Pierre Wolf<sup>1</sup>

<sup>1)</sup>*GAP-Biophotonics, Université de Genève, 1205 Geneva, Switzerland*

<sup>2)</sup>*Laboratorium für Physikalische Chemie, ETH Zürich, 8093, Zürich, Switzerland*

Sub- $\mu\text{m}$  thin samples are essential for spectroscopic purposes. The development of flat micro-jets enabled novel spectroscopic and scattering methods for investigating molecular systems in the liquid phase. However characterization of the temperature of these ultra-thin liquid sheets in vacuum has not been systematically investigated. Here we present a comprehensive temperature characterization of two methods producing sub-micron flatjets, using optical Raman spectroscopy: colliding of two cylindrical jets and a cylindrical jet compressed by a high pressure gas. Our results reveal the dependence of the cooling rate on the material properties and the source characteristics, i.e. nozzle orifice size, flowrate, pressure. We show that materials with higher vapour pressures exhibit faster cooling rates which is illustrated by comparing the temperature profile of liquid water and ethanol flatjets. In a sub- $\mu\text{m}$  liquid sheet, the temperature of the water sample reaches around 268 K and the ethanol around 253 K.

---

<sup>a)</sup>Electronic mail: yinz@ethz.ch

## I. INTRODUCTION

X-ray absorption spectroscopy (XAS) is a powerful method for the investigation of fundamental electronic properties of matter. However, the use of XAS in the soft X-rays is experimentally challenging in bulk materials, as transmission limits the sample thickness to some hundreds of nanometers.<sup>1</sup> This is especially true in liquids, for which geometrical effects and differences in absorption lengths can, in addition, lead to artifacts in the measured absorbance spectra.<sup>2,3</sup> Ultrathin liquid samples are also very valuable for other spectroscopic techniques like ultrafast MeV electron diffraction, which has the advantage of shorter wavelength and stronger interaction with matter than X-rays.<sup>4,5</sup> For MeV electron diffraction experiments in liquid samples, ultra-thin homogeneous samples are required to minimize noise contribution from inelastic electron scattering events. The small penetration depths of even high energetic electrons are  $<1 \mu\text{m}$  and thin samples with around 800 nm thickness are necessary to avoid multiple scattering events.<sup>6,7</sup>

Several methods have been developed to generate a sub-micron flat sheet in a vacuum environment, namely, two colliding cylindrical jets, 3D printed nozzles and gas-dynamic jets.<sup>8-10</sup> Earlier works of colliding jets have been performed under ambient conditions showing a thickness down to a  $\mu\text{m}$ .<sup>11-14</sup> Recent reported thicknesses reach 100 nm for both colliding jets and gas-dynamic jet.<sup>8-10,15</sup> These submicron-thickness flatjets have enabled several novel achievements in science, such as investigating liquid samples using high-order harmonic spectroscopy<sup>16,17</sup>, fs-transient XAS<sup>18</sup>, angular photoelectron spectroscopy<sup>19</sup>, and fs-electron scattering in liquids<sup>20</sup>. Despite these advantages and applications, an essential property of flatjets in vacuum, i.e. its temperature, remains mostly unknown.

Liquid samples in vacuum experience fast evaporation that result in a temperature decrease potentially reaching down to the supercooled regime.<sup>21-24</sup> For a majority of molecular systems, the temperature can have a vital impact on the properties and the evolution of the system. Although temperature characterization of super-cooled water droplets and cylindrical jets have been conducted in previous studies<sup>22,25-27</sup> using Raman spectroscopy, systematic investigation of liquid flatjets has not been performed yet. In this work, we present measurements of the temperature profiles of liquid water ( $\text{H}_2\text{O}$ ) and ethanol ( $\text{C}_2\text{H}_5\text{OH}$ ) in flatjets in vacuum using Raman spectroscopy. A systematic investigation of the temperature dependence on the material vapor pressure, nozzle orifice size, flowrate, and initial temperature

of the liquid sample is presented.

## II. EXPERIMENTAL METHODS

We investigated two types of flatjets: (1) a collision-based (impingement) flatjet formed by the collision of two cylindrical liquid jets<sup>8</sup>, and (2) a jet produced by a microfluidic nozzle, in which an initially cylindrical liquid jet is strongly compressed sideways by helium gas.<sup>10</sup> These two configurations are the two most widely used setups for liquid-phase XAS measurements. The determination of the temperature profiles within these liquid jets is therefore of key importance for spectroscopic investigations in the X-ray domain.

In both setups, we use a high-pressure liquid-chromatography (HPLC) pump to deliver the samples to the nozzles.<sup>18</sup> The vacuum in the experimental chamber typically ranges between  $5 \times 10^{-3}$  to  $1 \times 10^{-2}$  millibar during the measurements. In order to keep acceptable vacuum conditions, the sample is captured in a cold trap at liquid-nitrogen temperature. The investigated samples are distilled water and absolute pure ethanol with at least 99.8% purity (Merck).

For the collision-based flatjet<sup>8,16,18</sup>, two cylindrical liquid jets from two quartz nozzles of equal inner diameters (either 18  $\mu\text{m}$  or 60  $\mu\text{m}$ ) collide at an angle of  $48^\circ$  and generate a flatjet with a thickness that can be as thin as 500 nm, as assessed by white-light interferometry.

The thickness depends on several parameters, such as the orifice size of the nozzle, flowrate, type of liquid, and the measurement position. For the presented measurements, the flowrate was 2 ml/min for 18  $\mu\text{m}$  nozzles and 5 ml/min for 60  $\mu\text{m}$  nozzles, with a maximum jet velocity of 65.5 m/s and 14.7 m/s respectively.

For the gas-compressed flatjet, a microfluidic gas-dynamic chip nozzle from Micronit Microtechnologies BV with an orifice of 50  $\mu\text{m}$  was used.<sup>10</sup> The focusing gas was helium and its pressure was adjusted using a regulator between 5 and 10 bars. The liquid sample flowrate was 1 ml/min.

Fig. 1 illustrates our experimental scheme. As Raman excitation source, we used a Nd:YVO<sub>4</sub> cw laser (Coherent Verdi-V5) with a wavelength of 532 nm and a maximum power of 2W. Heating of the flatjet by this excitation laser is negligible as measurements performed at different pump powers showed negligible variations in flatjet temperature.

The Raman signal was collected at an angle of  $90^\circ$  with respect to the excitation beam

by an objective lens within the liquid-jet chamber. The collimated signal was then sent out of the chamber via a window and focused by another lens onto the entrance slit of a flat field spectrograph (Princeton Instruments Acton SP2300). The resulting spectrum was recorded by an EMCCD camera (Andor iXon3).

For the calibration of the temperature measurement using Raman scattering, we used the flatjet under ambient conditions and simultaneously measured its temperature with a thermocouple. The sample, liquid water, was either cooled with a cold bath or heated with a warm bath and a heating device coupled to the nozzle holder, in order to get an absolute and accurate calibration curve.

The Raman spectrum of liquid water around  $3400\text{ cm}^{-1}$  mainly consists in a superposition of five contributions (at  $3050$ ,  $3200$ ,  $3400$ ,  $3500$ , and  $3650\text{ cm}^{-1}$ ), which correspond to the fundamental O-H stretching bands, vibrations and Fermi resonances.<sup>28–30</sup> The intensity of each component changes relatively to the total intensity in response to temperature changes. For instance, with decreasing temperature, the integrated intensities of the  $3200$  and  $3400\text{ cm}^{-1}$  bands increase and that of the  $3500\text{ cm}^{-1}$  band decreases.

To obtain the calibration curve, we normalized the recorded Raman spectrum at the midpoint  $3300\text{ cm}^{-1}$  and integrated the total band area above and below  $3300\text{ cm}^{-1}$ . By plotting the ratio between these two integrated bands as a function of temperature, a calibration curve can be extracted by the expression<sup>22,23,26</sup>:

$$\frac{1}{T} = C_1 \ln \left( \frac{I_{<\Delta v}}{I_{>\Delta v}} \right) + C_2 \quad (1)$$

where  $T$  is the temperature,  $I_{<\Delta v}$  is the integrated intensity of the band below  $\Delta v = 3300\text{ cm}^{-1}$  and  $I_{>\Delta v}$  above it.  $C_1$  and  $C_2$  are empirical constants determined by calibration at known temperatures.

For the temperature measurements of ethanol, the anti-Stokes and Stokes signals could be recorded simultaneously so that the temperature was derived from the ratio of the two bands. A particularly well suited mode is the CCO symmetric stretch<sup>31</sup> at  $888.8\text{ cm}^{-1}$ . The temperature was thus extracted from the anti-Stokes/Stokes ratio:

$$\frac{I_{AS}}{I_S} = \left( \frac{V_l + V_{\Delta v}}{V_l - V_{\Delta v}} \right)^4 \exp \left( \frac{-hV_{\Delta v}}{kT} \right) \quad (2)$$

where  $T$  is the temperature,  $k$  the Boltzmann's constant,  $h$  the Planck's constant,  $V_l$  the

frequency of the laser and  $V_{\Delta v}$  the frequency of the CCO symmetric stretch mode (center frequency).

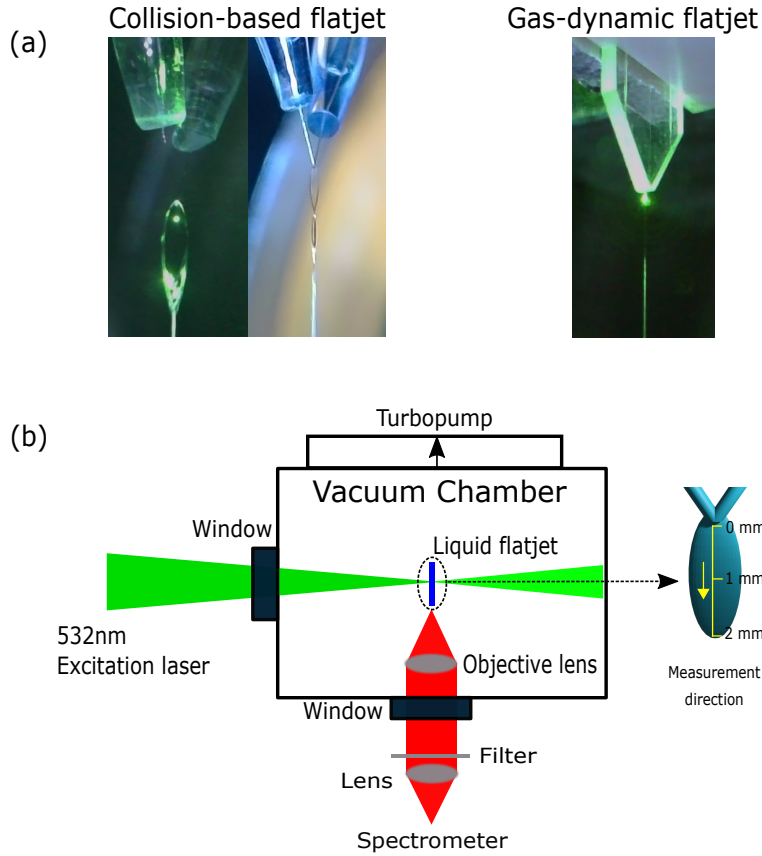


FIG. 1. Raman thermometry of liquid flatjets in vacuum. Two different flatjet methodologies are used: collision-based flatjets formed by colliding two cylindrical jets together at an angle of  $48^\circ$ , and gas-dynamic flatjets formed by using a focusing gas to compress a cylindrical liquid jet  $50\ \mu\text{m}$  in diameter into a flatjet. (a) For the measurements,  $18\ \mu\text{m}$  and  $60\ \mu\text{m}$  orifices are used for collision-based flatjets, and  $50\ \mu\text{m}$  orifice for gas-dynamic flatjets. (b) Top-down view of the sample chamber and a horizontal illustration of the flatjet. The flatjet is moved vertically within the chamber via an externally mounted manipulator and a cold trap attached below the sample chamber catches the remaining liquid.

### III. RESULTS AND DISCUSSION

Fig. 2 shows the temperature profile along the collision-based flatjets. The origin is set at the collision position. For liquid water flowing from the 18  $\mu\text{m}$  nozzles (blue curve), the maximum cooling of 25°C is obtained just before the end of the flat sheet, leading to a final temperature of  $\sim -2^\circ\text{C}$ . Due to the small nozzle diameter, only one flat sheet of about 1 mm length is formed.

For larger nozzle diameters (60  $\mu\text{m}$ ), the thickness of the flat sheet increases and the flow is more stable. This allows the formation of a second subsequent flat sheet, as shown in Fig. 2a (red and green curves). The first sheet is about 2 mm long and has a minimum temperature of  $\sim 8^\circ\text{C}$ . As it collapses into a single jet, temperature increases because of water masses from the rim of the flat sheet that now mixes with the central region. On the rim, the flatjet is thicker, less prone to evaporative cooling and warmer than the center. The second flat sheet is slightly shorter (about 1.5 mm), with a minimum temperature of  $\sim 2^\circ\text{C}$ . The overall cooling rate is thus lower for the 60  $\mu\text{m}$  nozzles (10 K/mm) than for the smaller 18  $\mu\text{m}$  nozzles (28 K/mm). This is consistent with the results from Ekimova et al.<sup>8</sup>, who estimated that evaporation yielded a mass loss of 5% under conditions comparable to ours, so that the thickness of the second flat sheet is still thicker than the single flat sheet from the 18  $\mu\text{m}$  nozzles. It has to be noticed, however, that the flowrates had to be adapted for obtaining stable jets for the 60  $\mu\text{m}$  (5 ml/min) and for the 18  $\mu\text{m}$  (2 ml/min) nozzles.

Interestingly supercooled water ( $-2^\circ\text{C}$ ) can thus be produced, when using collision-based flatjets with small nozzles. Supercooled water can, however, also be produced using 60  $\mu\text{m}$  nozzles, if the water is previously cooled at around 12  $^\circ\text{C}$  instead of room temperature, as shown by the green plot in Fig. 2a. Moreover the length of the cold region zone is extended over several mm.

As compared to water, ethanol experienced a much stronger cooling rate (Fig. 2b), due to its faster evaporation. Even with the 60  $\mu\text{m}$  nozzles, an average cooling rate of  $\sim 29$  K/mm is observed, which is 3 times faster than water under the same conditions. Only one sheet can be formed due to the loss of matter, and the lowest temperature found in this sheet reaches  $-20^\circ\text{C}$ . For the same reason, a stable flatjet of alcohol was difficult to produce when using the smaller nozzles.

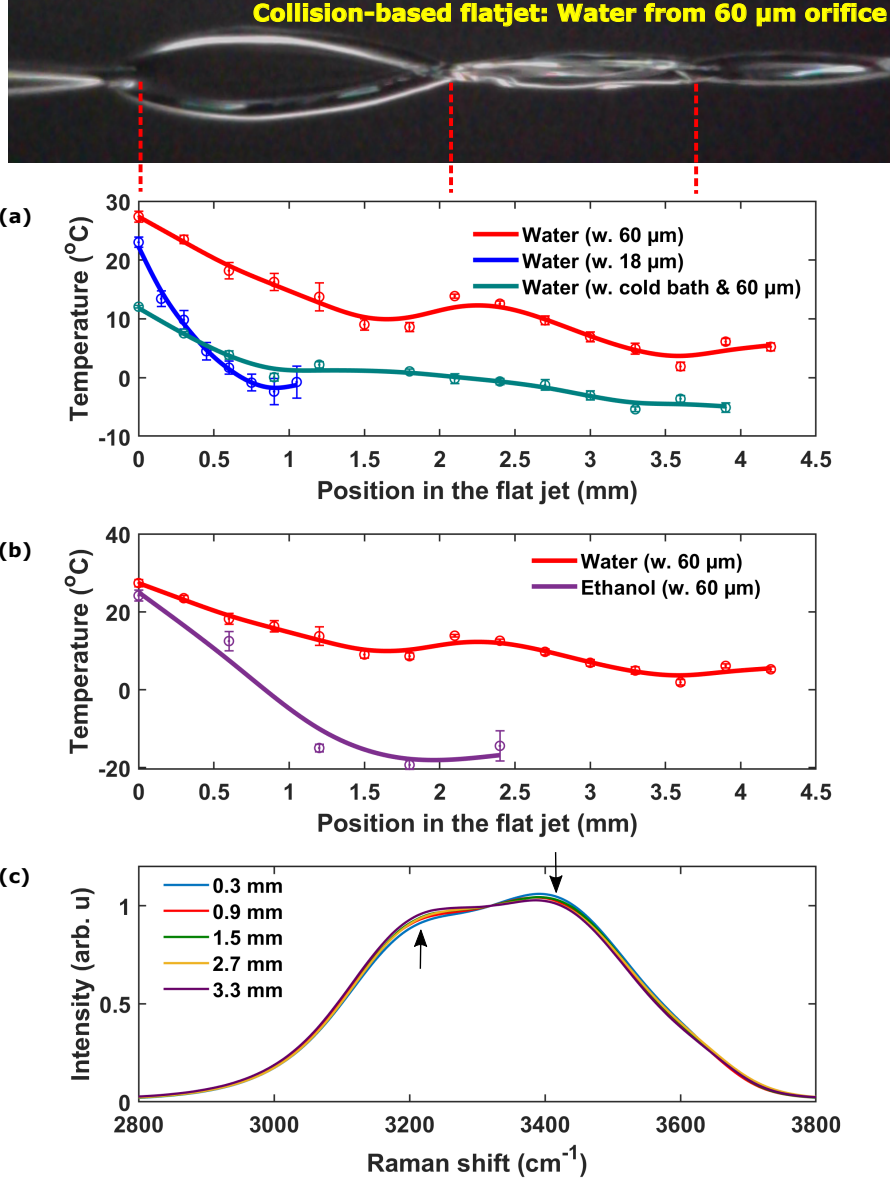


FIG. 2. Measurements with collision-based flatjets of different samples under different initial temperature, flowrate and orifice size, starting from an initial position defined as 0mm just below the collision point as indicated by the red dashed line. a) Thermal profiles of water using 18  $\mu\text{m}$  nozzles at 2 ml/min (Blue), water using 60  $\mu\text{m}$  nozzles at 5 ml/min (Red), and water using 60  $\mu\text{m}$  nozzles at 5 ml/min with an initial temperature of 12  $^{\circ}\text{C}$  maintained by placing the sample in an external cold-bath (Green). b) Thermal profile of ethanol using 60  $\mu\text{m}$  nozzles at 5 ml/min (Purple) as measured via the stokes/anti-stokes ratio. c) Raman spectra of liquid water at different positions along the flatjet of water in cold-bath.

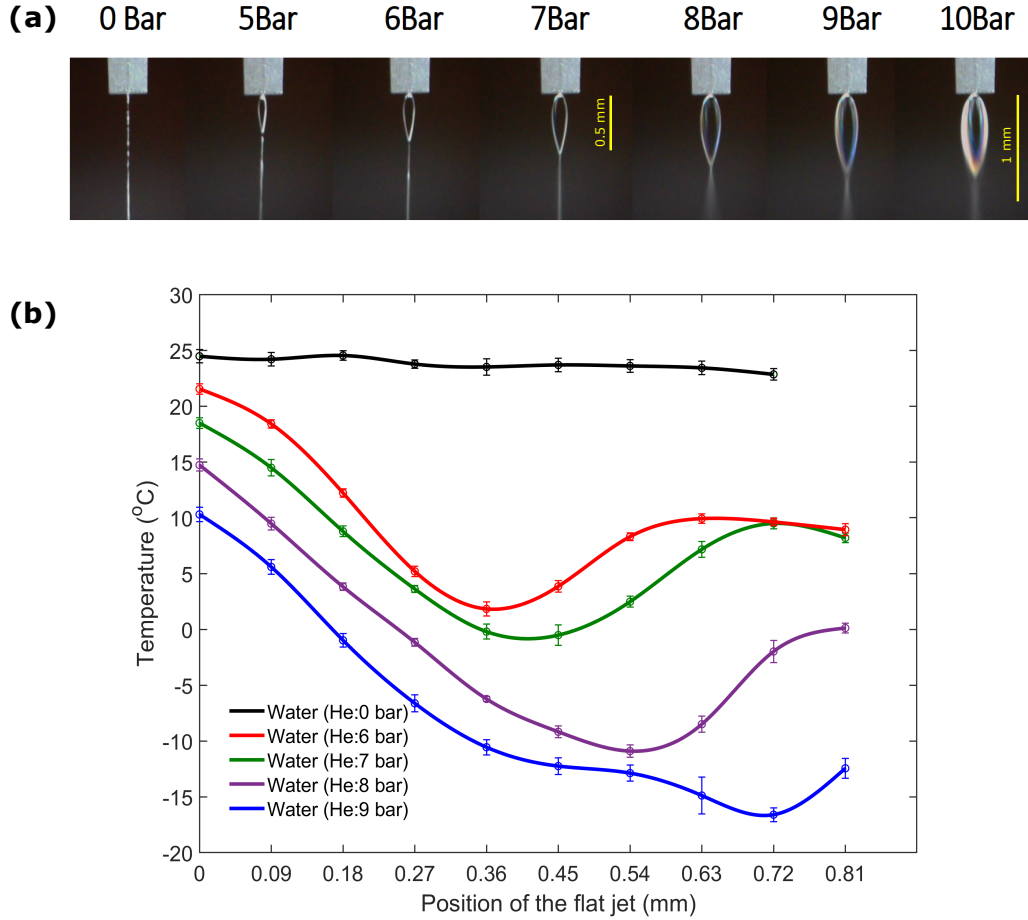


FIG. 3. Measurements with a microfluidic gas-dynamic chip nozzle. a) Gas-dynamic flatjets generated with different focusing gas pressure from 5-10 bar of helium, at a constant flowrate of 1 ml/min. A lower liquid flowrate is required for operation compared to collision-based flatjets, therefore much smaller flatjets are formed.<sup>10</sup> b) Thermal profiles of the gas-dynamic flatjets, at an initial position defined as 0 mm just below the nozzle tip.

For the gas-dynamic flatjet, as shown in Fig. 3, the measurements start at approximately 0.1 mm just below the nozzle. Note that the focusing gas starts compressing the liquid sample in the nozzle tip itself. By holding the flowrate constant at 1 ml/min and increasing the gas pressure, one observes an increase in the flatjet size up to 10 bar, at which point the flatjet starts disintegrating. The overall flat sheet is also much shorter than for the colliding-jet source, with a maximum length of about 1 mm. As shown in Table I, for gas pressures of 6-9 bar, the cooling rates reach as much as 54.7, 51.9, 52.6 and 58.1 K/mm, respectively and an initial exit temperature of 21.5, 18.4, 14.7 and 10.3 °C, respectively. While the



TABLE I. Gas-dynamic flatjets: experimental values of the exit temperature (temperature at the highest point of the flatjet) and average cooling rate for different focusing gas pressure. The maximum jet velocity of the flatjet is 8.5 m/s.

Gas pressure (bar)	Flowrate (ml min <sup>-1</sup> )	Exit temperature (°C)	Avg. Cooling rate (°C mm <sup>-1</sup> )
6.00	1.00	21.5	54.7
7.00	1.00	18.4	51.9
8.00	1.00	14.7	52.6
9.00	1.00	10.3	58.1

average cooling rate appears to have little-to-no dependence on the focusing gas pressure, the initial exit temperature is strongly dependent on it. This suggests that while the use of a focusing gas limits the effect of evaporative cooling, heat is still lost through conductive cooling between the gas and liquid.

#### IV. MODEL CALCULATIONS

To explain the thermal evolution of the colliding flatjet, we developed a basic model to fit our measurements. No modeling was performed on the gas-dynamic flatjet experiment, due to its complex geometry and some unknown geometrical parameters in this commercial device. To begin, we use the Hertz-Knudsen equation to describe the mass flux  $J_{HK}$  from a liquid surface, which is generally given in the form<sup>32,33</sup>:

$$J_{HK} = \frac{1}{A} \frac{dN}{dt} = \frac{\alpha_s}{\sqrt{2\pi m k_B}} \left( \frac{\sigma_e P_S}{\sqrt{T_{I,L}}} - \frac{\sigma_c P_V}{\sqrt{T_{I,V}}} \right) \quad (3)$$

where  $A$  is the area,  $N$  is the number of molecules,  $k_B$  is the Boltzmann constant,  $T_{I,L}/T_{I,V}$  is the interfacial liquid/vapor temperature,  $m$  is the mass of a molecule,  $P_S$  is the saturation vapor pressure,  $P_V$  is the gas pressure,  $\sigma_e$  is the evaporation coefficient,  $\sigma_c$  is the condensation coefficient, and  $\alpha_s$  is the sticking coefficient of the gas onto a surface.

In addition, the change in temperature  $dT$  due to the phase transition (evaporative cooling) of  $dN$  molecules is given by

$$dT = \frac{H_v}{N_A C_m M V} dN \quad (4)$$

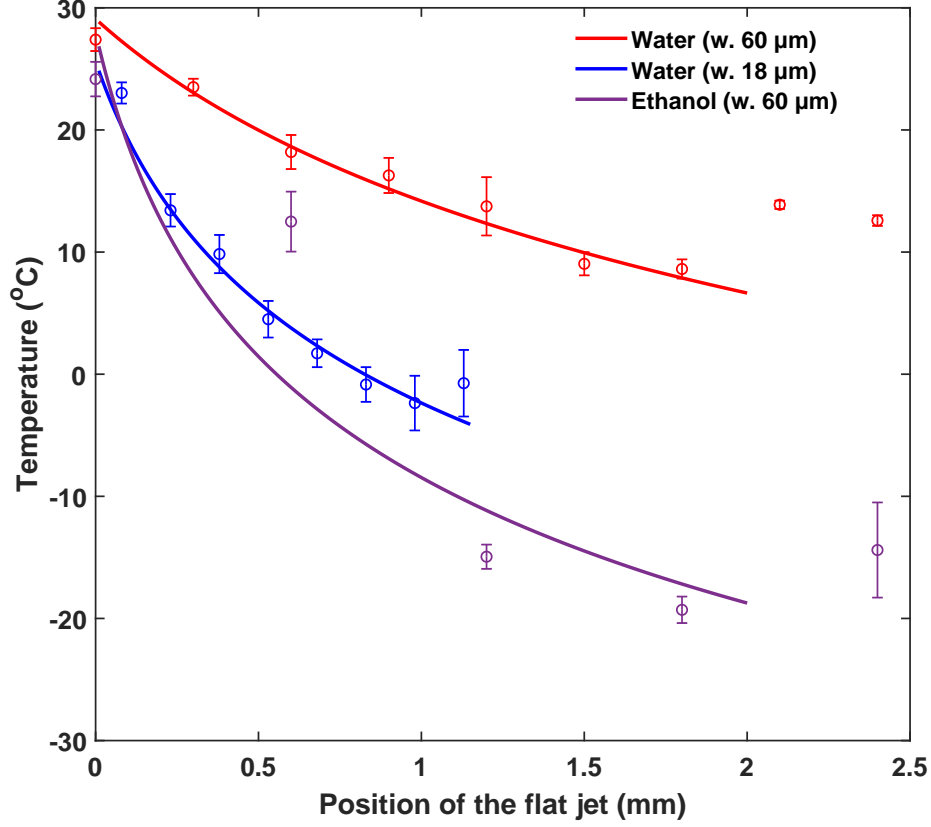


FIG. 4. Fitting of experimental data through numerical integration of Eq. 8a. Blue: water with 18  $\mu\text{m}$  nozzles. Red: water with 60  $\mu\text{m}$  nozzles. Purple: ethanol with 60  $\mu\text{m}$  nozzles.

where  $H_v$  is the evaporation enthalpy,  $N_A$  is the Avogadro constant,  $C_m$  is the molar specific heat,  $M$  is the molar density,  $V$  is the volume of the liquid.

Combining Eq. 3 and Eq. 4 yields the following expression for the change in temperature

per unit length of the liquid jet in the vertical z-axis (i.e. cooling rate):

$$\begin{aligned}
\frac{dT}{dz} &= -\frac{H_v}{N_A C_m M V} \frac{dN}{dt} \frac{dt}{dz} \\
&= -\frac{H_v}{N_A C_m M V} \frac{2A J_{HK}}{v_z} \\
&= -\frac{2H_v}{N_A C_m M l_j(z)} \frac{J_{HK}}{v_z}
\end{aligned} \tag{5}$$

where  $l_j$  is the thickness of the jet and  $v_z$  is the velocity of the jet along the z-axis.

The thickness of the jet has been estimated by Hasson and Peck<sup>11,34</sup> as:

$$l_j(z) = \Lambda \frac{d_o^2}{4z} \frac{\sin^3(\phi)}{(1 + \cos(\theta) \cos(\phi))^2} = \frac{l_0}{z}; \tag{6}$$

where  $z$  is the distance from the collision point,  $d_o$  is the orifice diameter,  $2\phi = 48^\circ$  is the collision angle,  $\theta = 0^\circ$  is the azimuthal angle,  $\Lambda$  is an unitless proportionality constant, and  $l_0$  is the overall proportionality constant ( $m^2$ ) at fixed  $\phi$  and  $\theta$ . From white-light interferometric measurements of the flat jet thickness, a value of  $\Lambda = 124$  is obtained as the best fit. Equation 6 predicts a linear decrease of the jet thickness with the distance from the collision point. However, it has been observed in our and other experiments<sup>8,15,16</sup> that not only is the boundary rim of the flat sheet substantially thicker than its center, the size of the flat sheet also varies with the flowrate of the liquid jet, which is not captured by Eq. 6. While more complex models that take into account these effects exist<sup>35,36</sup>, we decided that for our measurements along the center of the sheet, Eq. 6 was reasonably applicable once minor corrections were made.

Although the Hertz-Knudsen (HK) model is perfectible<sup>33,37</sup>, we used a simplified evaporation flux model  $J_\gamma$ , based on the HK equation, where the equilibrium/saturation vapor pressure  $P_v$  is given by the Clausius–Clapeyron equation:

$$\begin{aligned}
J_\gamma &= \frac{\gamma P_v}{\sqrt{2\pi m k_B T}} \\
&= \frac{\gamma P_{ref}}{\sqrt{2\pi m k_B T}} \exp \left[ -\frac{H_v}{k_B T_{ref}} \left( \frac{T_{ref} - T}{T} \right) \right] \\
&= \gamma \frac{J_0}{\sqrt{T}} \exp \left[ -\frac{H_v}{k_B T_{ref}} \left( \frac{T_{ref} - T}{T} \right) \right]
\end{aligned} \tag{7}$$

where  $T_{ref} = 298.15\text{K}$  is the reference temperature,  $P_{ref}$  is the vapor pressure at  $T_{ref}$ ,  $\gamma$  is an unitless proportionality constant and  $J_0 = P_{ref}/\sqrt{2\pi mk_B}$ . From Eq. 7, we define our final simplified fitting model by:

$$\begin{aligned} \frac{dT}{dz} &= -\frac{2H_v}{N_A C_m M l_j(z)} \frac{J_\gamma}{v_z} F(z) \\ &= -2\gamma\epsilon \frac{H_v}{N_A C_m M l_0 v_z} \frac{J_0}{\sqrt{T}} \exp\left[-\frac{H_v}{k_B T_{ref}} \left(\frac{T_{ref} - T}{T}\right)\right] \\ &= -\frac{\alpha C}{\sqrt{T}} \exp\left[-\frac{H_v}{k_B T_{ref}} \left(\frac{T_{ref} - T}{T}\right)\right] \end{aligned} \quad (8a)$$

with

$$F(z) = \frac{\epsilon}{z} \quad (8b)$$

$$C = \frac{H_v J_0}{N_A C_m M l_0 v_z} \quad (8c)$$

where  $\alpha = 2\gamma\epsilon$  is an overall proportionality constant with dimension  $m$ , with  $\epsilon$  a correction constant, and  $C$  is the cooling coefficient.  $F(z)$  is a correction function for the flatjet's geometric properties. The fits to the experimental data obtained from numerical integration of Eq. 8a are presented in Fig. 4.

TABLE II. Proportionality constants  $\alpha$  are unknown variables obtained from fittings of the experimental data with numerical integration of Eq. 8a. Cooling coefficients  $C$  are known variables that can be calculated from experimental parameters and provide an estimation for the cooling rate of an unknown sample relative to a known one.

Sample (Orifice diameter)	Flowrate (ml min <sup>-1</sup> )	$\alpha$ (m)	$C$ (K <sup>1.5</sup> m <sup>-2</sup> )
H <sub>2</sub> O (18 $\mu\text{m}$ )	2.00	4.00E-04	3.19E+09
H <sub>2</sub> O (60 $\mu\text{m}$ )	5.00	2.55E-04	1.28E+09
C <sub>2</sub> H <sub>5</sub> OH (60 $\mu\text{m}$ )	5.00	4.65E-04	3.67E+09

As listed in Table II, different values of  $\alpha$  and cooling coefficient  $C$  are given for the three different cases of water from 18  $\mu\text{m}$ , water from 60  $\mu\text{m}$  and ethanol from 60  $\mu\text{m}$  orifices. The ratio of the average experimental cooling-rate for different measurement sets can be approximately expressed as a ratio of cooling coefficients  $C'/C$ .

According to Eq. 8c, although the cooling coefficient is not directly dependent on the nozzle orifice-diameter (given Eq. 6), it is inversely proportional to the jet velocity and

therefore the flowrate, which is orifice-diameter dependent. Experimentally, flowrates of 2 and 5 ml min<sup>-1</sup> were used for 18 μm and 60 μm orifices respectively, with an experimental cooling-rate ratio of ~3, compared to  $C_{18\mu m}^{H_2O}/C_{60\mu m}^{H_2O} = 2.5$ . Given that the flatjets are only stable within a small flowrate range for a given orifice size, and that their areas depend on the flowrate, it was experimentally difficult to observe a flowrate dependence for a fixed orifice. The cooling coefficient ratio for ethanol/water is  $C_{60\mu m}^{EtOH}/C_{60\mu m}^{H_2O} = 2.87$ , which is similar to the experimental cooling-rate ratio of ~2.9.

For the thermal evolution of the gas-dynamic flatjet, an alternative model to the colliding jet would need to be developed. Such a model would need to take into account not just evaporative cooling, but also the strong likelihood of conductive cooling between the compression gas and sample liquid. This may be explored in a future study. From the measurements, it can be concluded that the focusing gas does not prevent the liquid sample from cooling. The use of the gas-compressed flatjet to reach the deeply supercooled regime of water is left for future studies.<sup>27</sup>

## V. CONCLUSION

In conclusion, we have measured the thermal profiles of two different types of liquid flat-jet systems in vacuum utilizing optical Raman spectroscopy and observed the temperature dependence on the material vapour pressure, orifice size, flowrate and initial temperature of the liquid sample. Lower temperatures are accessible in water with the gas-compressed flat-jet than the collision-based flatjet. Based on the results, we developed a simplified, empirical model to describe the effect of evaporative cooling on collision-based flatjets. In addition, we demonstrated that liquid water in the flatjets can enter the supercooled regime, which opens up future investigations of the supercooled water using transient XAS, HHG spectroscopy, electron diffraction, attosecond spectroscopy<sup>38</sup> and many more. More generally, the measurements reported herein will facilitate the first systematic temperature-dependent studies of liquid-phase systems using these novel techniques.

## ACKNOWLEDGEMENTS

Acknowledgements: It is our pleasure to thank Andreas Schneider, Mario Seiler, Andres Laso, and Markus Kerellaj for their contributions to the construction of the experiment and Michel Moret for his precious technical assistance. This work was supported by ETH Zurich, the Swiss National Science Foundation (SNSF) through the NCCR-MUST and project (No 20021-172946) and an ERC Consolidator Grant (No 772797-ATTOLIQ). T.B. acknowledges financial support from a Marie-Curie fellowship grant agreement No 798176. Z.Y. acknowledges financial support from an ETH Career Seed Grant No SEED-12 19-1/1-004952-000.

## AUTHOR DECLARATIONS

### Conflict of Interest

The authors have no conflicts to disclose.

## DATA AVAILABILITY

The data that support the findings of this study are available from the corresponding authors upon reasonable request.

## REFERENCES

- <sup>1</sup>J. W. Smith and R. J. Saykally, “Soft x-ray absorption spectroscopy of liquids and solutions,” *Chemical reviews* **117**, 13909–13934 (2017).
- <sup>2</sup>S. Eisebitt, T. Böske, J.-E. Rubensson, and W. Eberhardt, “Determination of absorption coefficients for concentrated samples by fluorescence detection,” *Physical Review B* **47**, 14103 (1993).
- <sup>3</sup>P. Busse, Z. Yin, D. Mierwaldt, J. Scholz, B. Kressdorf, L. Glaser, P. S. Miedema, A. Rothkirch, J. Viefhaus, C. Jooss, *et al.*, “Probing the surface of  $\text{LaO}_2$  on  $\text{SrTiO}_3$  in water vapor by in situ photon-in/photon-out spectroscopy,” *The Journal of Physical Chemistry C* **124**, 7893–7902 (2020).

- <sup>4</sup>J. Nunes, K. Ledbetter, M. Lin, M. Kozina, D. DePonte, E. Biasin, M. Centurion, C. Crisman, M. Dunning, S. Guillet, *et al.*, “Liquid-phase mega-electron-volt ultrafast electron diffraction,” *Structural Dynamics* **7**, 024301 (2020).
- <sup>5</sup>J. Yang, X. Zhu, J. P. F. Nunes, J. K. Yu, R. M. Parrish, T. J. Wolf, M. Centurion, M. Gühr, R. Li, Y. Liu, B. Moore, M. Niebuhr, S. Park, X. Shen, S. Weathersby, T. Weinacht, T. J. Martinez, and X. Wang, “Simultaneous observation of nuclear and electronic dynamics by ultrafast electron diffraction,” *Science* **368**, 885–889 (2020).
- <sup>6</sup>D. DePonte, J. Mckeown, U. Weierstall, R. Doak, and J. Spence, “Towards etem serial crystallography: Electron diffraction from liquid jets,” *Ultramicroscopy* **111**, 824–827 (2011).
- <sup>7</sup>A. Akar, H. Gümüş, and N. T. Okumuşoğlu, “Electron inelastic mean free path formula and csda-range calculation in biological compounds for low and intermediate energies,” *Applied radiation and isotopes* **64**, 543–550 (2006).
- <sup>8</sup>M. Ekimova, W. Quevedo, M. Faubel, P. Wernet, and E. T. J. Nibbering, “A liquid flatjet system for solution phase soft-x-ray spectroscopy.” *Structural dynamics (Melville, N.Y.)* **2**, 054301 (2015).
- <sup>9</sup>G. Galinis, J. Strucka, J. C. T. Barnard, A. Braun, R. A. Smith, and J. P. Marangos, “Micrometer-thickness liquid sheet jets flowing in vacuum,” *Review of Scientific Instruments* **88**, 083117 (2017), <https://doi.org/10.1063/1.4990130>.
- <sup>10</sup>J. D. Koralek, J. B. Kim, P. Brůža, C. B. Curry, Z. Chen, H. A. Bechtel, A. A. Cordones, P. Sperling, S. Toleikis, J. F. Kern, S. P. Moeller, S. H. Glenzer, and D. P. DePonte, “Generation and characterization of ultrathin free-flowing liquid sheets,” *Nature Communications* **9**, 1353 (2018).
- <sup>11</sup>G. Taylor, “Formation of thin flat sheets of water,” *Proceedings of the Royal Society of London. Series A. Mathematical and Physical Sciences* **259**, 1–17 (1960), <https://royalsocietypublishing.org/doi/pdf/10.1098/rspa.1960.0207>.
- <sup>12</sup>K. D. Miller Jr, “Distribution of spray from impinging liquid jets,” *Journal of Applied Physics* **31**, 1132–1133 (1960).
- <sup>13</sup>J. Huang, “The break-up of axisymmetric liquid sheets,” *Journal of Fluid Mechanics* **43**, 305–319 (1970).
- <sup>14</sup>N. Bremond and E. Villermaux, “Atomization by jet impact,” *Journal of Fluid Mechanics* **549**, 273–306 (2006).

- <sup>15</sup>Z. Yin, T. T. Luu, and H. J. Wörner, “Few-cycle high-harmonic generation in liquids: in-operando thickness measurement of flat microjets,” *Journal of Physics: Photonics* **2**, 044007 (2020).
- <sup>16</sup>T. T. Luu, Z. Yin, A. Jain, T. Gaumnitz, Y. Pertot, J. Ma, and H. J. Wörner, “Extreme-ultraviolet high-harmonic generation in liquids,” *Nature Communications* **9**, 3723 (2018).
- <sup>17</sup>V. Svoboda, Z. Yin, T. T. Luu, and H. J. Wörner, “Polarization measurements of deep-to extreme-ultraviolet high harmonics generated in liquid flat sheets,” *Opt. Express* **29**, 30799–30808 (2021).
- <sup>18</sup>A. D. Smith, T. Balciunas, Y.-P. Chang, C. Schmidt, K. Zinchenko, F. B. Nunes, E. Rossi, V. Svoboda, Z. Yin, J.-P. Wolf, and H. J. Wörner, “Femtosecond soft-x-ray absorption spectroscopy of liquids with a water-window high-harmonic source,” *The Journal of Physical Chemistry Letters* **11**, 1981–1988 (2020).
- <sup>19</sup>S. Malerz, H. Haak, F. Trinter, A. Stephansen, C. Kolbeck, M. Pohl, U. Hergenhahn, G. Meijer, and B. Winter, “A setup to measure photoelectron circular dichroism from chiral molecules in aqueous solution,” arXiv preprint arXiv:2109.14365 (2021).
- <sup>20</sup>M.-F. Lin, N. Singh, S. Liang, M. Mo, J. Nunes, K. Ledbetter, J. Yang, M. Kozina, S. Weathersby, X. Shen, *et al.*, “Imaging the short-lived hydroxyl-hydronium pair in ionized liquid water,” *Science* **374**, 92–95 (2021).
- <sup>21</sup>J. A. Sellberg, C. Huang, T. A. McQueen, N. Loh, H. Laksmono, D. Schlesinger, R. Sierra, D. Nordlund, C. Hampton, D. Starodub, *et al.*, “Ultrafast x-ray probing of water structure below the homogeneous ice nucleation temperature,” *Nature* **510**, 381–384 (2014).
- <sup>22</sup>C. Goy, M. A. Potenza, S. Dederà, M. Tomut, E. Guillermin, A. Kalinin, K.-O. Voss, A. Schottelius, N. Petridis, A. Prosvetov, *et al.*, “Shrinking of rapidly evaporating water microdroplets reveals their extreme supercooling,” *Physical review letters* **120**, 015501 (2018).
- <sup>23</sup>K. R. Wilson, B. S. Rude, J. Smith, C. Cappa, D. Co, R. Schaller, M. Larsson, T. Catalano, and R. Saykally, “Investigation of volatile liquid surfaces by synchrotron x-ray spectroscopy of liquid microjets,” *Review of scientific instruments* **75**, 725–736 (2004).
- <sup>24</sup>A. Charvat, E. Lugovoj, M. Faubel, and B. Abel, “New design for a time-of-flight mass spectrometer with a liquid beam laser desorption ion source for the analysis of biomolecules,” *Review of scientific instruments* **75**, 1209–1218 (2004).



- <sup>25</sup>M. Faubel, S. Schlemmer, and J. P. Toennies, “A molecular beam study of the evaporation of water from a liquid jet,” *Zeitschrift für Physik D Atoms, Molecules and Clusters* **10**, 269–277 (1988).
- <sup>26</sup>J. D. Smith, C. D. Cappa, W. S. Drisdell, R. C. Cohen, and R. J. Saykally, “Raman thermometry measurements of free evaporation from liquid water droplets,” *Journal of the American Chemical Society* **128**, 12892–12898 (2006).
- <sup>27</sup>R. E. Grisenti, A. Kalinin, C. Goy, and A. Schottelius, “Evaporating laminar microjets for studies of rapidly evolving structural transformations in supercooled liquids,” *Advances in Physics: X* **3**, 1418183 (2018), <https://doi.org/10.1080/23746149.2017.1418183>.
- <sup>28</sup>W. B. Monosmith and G. E. Walrafen, “Temperature dependence of the raman oh-stretching overtone from liquid water,” *The Journal of Chemical Physics* **81**, 669–674 (1984), <https://doi.org/10.1063/1.447748>.
- <sup>29</sup>H. Suzuki, Y. Matsuzaki, A. Muraoka, and M. Tachikawa, “Raman spectroscopy of optically levitated supercooled water droplet,” *The Journal of Chemical Physics* **136**, 234508 (2012), <https://doi.org/10.1063/1.4729476>.
- <sup>30</sup>Q. Sun, “Local statistical interpretation for water structure,” *Chemical Physics Letters* **568**, 90–94 (2013).
- <sup>31</sup>A. Emin, A. Hushur, and T. Mamtimin, “Raman study of mixed solutions of methanol and ethanol,” *AIP Advances* **10**, 065330 (2020), <https://doi.org/10.1063/1.5140722>.
- <sup>32</sup>M. Knudsen and J. R. Partington, “The kinetic theory of gases. some modern aspects,” *The Journal of Physical Chemistry* **39**, 307–307 (1935), <https://doi.org/10.1021/j150362a021>.
- <sup>33</sup>A. H. Persad and C. A. Ward, “Expressions for the evaporation and condensation coefficients in the hertz-knudsen relation,” *Chemical Reviews* **116**, 7727–7767 (2016), PMID: 27314250, <https://doi.org/10.1021/acs.chemrev.5b00511>.
- <sup>34</sup>D. Hasson and R. E. Peck, “Thickness distribution in a sheet formed by impinging jets,” *AICHE Journal* **10**, 752–754 (1964), <https://aiche.onlinelibrary.wiley.com/doi/pdf/10.1002/aic.690100533>.
- <sup>35</sup>J. W. M. Bush and A. E. Hasha, “On the collision of laminar jets: fluid chains and fishbones,” *Journal of Fluid Mechanics* **511**, 285–310 (2004).
- <sup>36</sup>Y. J. Choo and B. S. Kang, “The effect of jet velocity profile on the characteristics of thickness and velocity of the liquid sheet formed by two impinging jets,” *Physics of Fluids* **19**, 112101 (2007), <https://doi.org/10.1063/1.2795780>.

- <sup>37</sup>R. Hołyst, M. Litniewski, and D. Jakubczyk, “A molecular dynamics test of the hertz–knudsen equation for evaporating liquids,” *Soft Matter* **11**, 7201–7206 (2015).
- <sup>38</sup>I. Jordan, M. Huppert, D. Rattenbacher, M. Peper, D. Jelovina, C. Perry, A. V. Conta, A. Schild, and H. J. Wörner, “Attosecond spectroscopy of liquid water,” *Science* **369**, 974–979 (2020).